Comparative Assessment of Nine Scatter Correction Methods Based on Spectral Analysis Using Monte Carlo Simulations

Irène Buvat, Mercedes Rodriguez-Villafuerte, Andrew Todd-Pokropek, Habib Benali and Robert Di Paola

U66 INSERM, Institut Gustave-Roussy, Villejuif, France; and Department of Medical Physics, University College London, London, United Kingdom

We compared nine scatter correction methods based on spectral analysis which process SPECT projections. **Methods:** Monte Carlo simulation was used to generate histories of photons emitted from a realistic ^{99m}Tc phantom. A particular projection was considered. Information regarding the history, location and energy of the photons detected in this projection was analyzed to test the assumptions underlying each scatter correction method. Relative and absolute quantification and signal-to-noise ratio were assessed for each scatter corrected image. **Results:** For the simulated data, two methods do not enable activity quantification. Among the methods requiring some parameters to be calibrated, the dual-energy window method shows the best compromise between accuracy and ease of implementation but introduces a bias in relative quantification. In this respect, a triple-energy window technique is more accurate than the dual-window method. A factor analysis approach results in more stable quantitative accuracy (error ~10%) for a wide range of activity but requires a more sophisticated acquisition mode (30 energy windows). **Conclusion:** These results show that a scatter correction method using spectral analysis can be used to substantially improve accurate quantification.

Key Words: scatter correction; single-photon emission computed tomography; spectral analysis

J Nucl Med 1995; 36:1476–1488

Accurate quantification in SPECT is affected by the characteristics of the SPECT system (energy and spatial resolution, mechanical stability, sensitivity, uniformity of the response, etc.), by some physical phenomena (scatter, attenuation, septal penetration, partial volume effect), by tomographic reconstruction and by physiological factors (patient motion). In all these factors, the problem of scatter has given rise to many investigations due to its blurring effect. As scattered photons are detected at a location which corresponds roughly to the location of their last scatter interaction, they convey poor information regarding their emission position. Consequently, their inclusion in the image affects contrast, spatial resolution and quantification. Many scatter correction methods have been described (*1*). Some of them perform a spatial analysis by using deconvolution procedures. Others rely on a spectral analysis (i.e., process energy information). This work investigates the performance of nine scatter correction methods based on spectral analysis. They differ in their underlying hypotheses and in the complexity of their implementation. The aim of this study is to look into the validity of the assumptions of these methods and their potential in terms of relative and absolute activity quantification, and signal-to-noise ratio.

An objective assessment of scatter correction methods requires knowing the spatial distribution of unscattered and scattered photons. Monte Carlo modeling of gamma-ray transport has been established as a useful technique for simulating realistic SPECT data while controlling the characteristics related to the "detected" photons, especially their emission and detection locations and the interactions they have undergone (*2*). In SPECT, however, the combination of errors due to physical and algorithmic effects makes it difficult to analyze the precise origin of errors observed on reconstructed slices. Because all scatter corrections evaluated in this work process projections before reconstruction is performed, they have been compared using a Monte Carlo simulated projection of a physical phantom. Since the projection of only the unscattered photons is available, the accuracy of the scatter correction methods can be evaluated by examining both the validity of their assumptions and their ability to properly estimate the spatial distribution of unscattered photons in the projection.

MATERIALS AND METHODS

Monte Carlo Simulation

The Monte Carlo simulation was developed using the general-purpose EGS4 code system (*3*). The software described the transport of photons and included Compton scatter, coherent scatter and photoelectric effect (*4*). It was designed for simulating a NaI(Tl) SPECT detector with a low-energy, high-resolution, parallel-hole collimator. The intrinsic energy response of the detector was modeled by Gaussian functions, assuming the following rela-

Received Jun. 29, 1994; revision accepted Dec. 28, 1994.

For correspondence or reprints contact: Irène Buvat, U66 INSERM, Institut Gustave-Roussy, 39 rue Camille Desmoulins, 94 805 Villejuif Cedex, France.

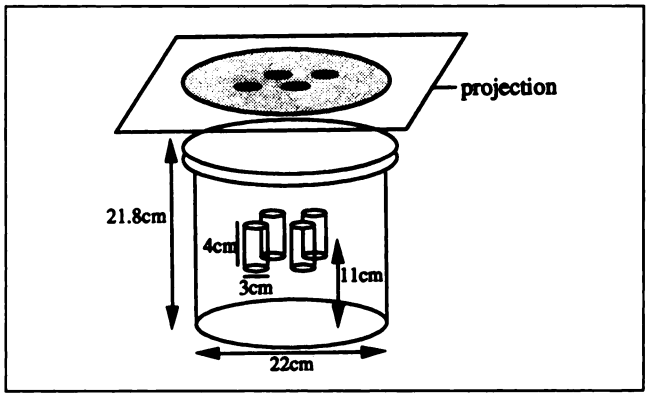

FIGURE 1. Simulated phantom and projection. Relative activity concentrations of the small cylinders with respect to the background were 2, 4, 6 and 8.

tionship between the FWHM of the Gaussian response and the energy, E, of the primary photons (*5*):

$$FWHM = \sqrt{\alpha + \beta E}, \qquad \text{Eq. 1}$$

with α and β equal to 20.42 and 1.3027, respectively. Those values were representative of experimental measurements of energy resolution. A perfect intrinsic spatial resolution was simulated.

The simulated phantom consisted of four equal-sized cylinders embedded in a cylindrical phantom containing a uniform background of ^{99m}Tc (Fig. 1). Relative ^{99m}Tc activity concentrations of the four hot small cylinders with respect to the background were 2, 4, 6 and 8, respectively.

The projection for which the head of the camera was parallel to the top of the phantom and in contact with it was considered (Fig. 1). The simulated data were recorded in a list mode. For each detected photon, its emission and detection locations, energy of detection and the number of Compton and Rayleigh interactions it had undergone were stored. Every photon detected with an energy within a 60–180-keV range was considered. Three million events were acquired. For each scatter correction method, the list mode was processed and the data were sorted to get the image or the set of images corresponding to the energy ranges required by the method. The image matrix was 64 × 64 with a pixel size equal to 0.39 × 0.39 cm^2. The images of the unscattered and scattered photons were also created.

Scatter Correction Methods

Nine scatter correction methods (referred to as M1 to M9, presented below) were assessed. For each of them, the underlying hypotheses are emphasized. The methodologies used to optimize the required parameters and to study the validity of the hypotheses are described.

M1: Photopeak Window Acquisition. A conventional 126–154-keV image corresponding to the 20% spectral window centred on 140 keV was created. This spectral window will be subsequently referred to as the photopeak window. The number of unscattered photons detected outside this window was determined, as well as the number of scattered photons included within this window.

M2: Dual-Photopeak Window Method. This method (*6*) assumes an existing relationship between the scatter fraction in the pixel i, SF(i) and the ratio of the number of counts detected in two equally wide subwindows splitting the photopeak window:

$$SF(i) = A[I_{lw}(i)/I_{uw}(i)]^B + C, \qquad \text{Eq. 2}$$

where $I_{lw}(i)$ and $I_{uw}(i)$ are the numbers of counts detected in the pixel i in the lower and upper subwindows, respectively. As the scatter fraction is related to the scatter-to-total ratio, the number of scattered photons, $S_{pk}(i)$, detected in a pixel i in the photopeak window can be estimated once A, B and C have been calibrated using (*6*):

$$\hat{S}_{pk}(i) = I(i)SF(i)/[1 + SF(i)], \qquad \text{Eq. 3}$$

where $I(i) = I_{lw}(i) + I_{uw}(i)$ is the number of photons detected in the pixel i in the photopeak window and $\hat{}$ denotes the estimated quantities. The estimated image of unscattered photons in the photopeak window, $\hat{U}_{pk}$, is then deduced by:

$$\hat{U}_{pk}(i) = I(i) - \hat{S}_{pk}(i). \qquad \text{Eq. 4}$$

The method requires calibration of A, B and C. To determine these parameters, the exact values of $SF(i) = S_{pk}(i)/U_{pk}(i)$ were calculated and plotted against $R(i) = I_{lw}(i)/I_{uw}(i)$. A nonlinear regression analysis was performed using the pixels included in two different regions of interest (ROIs). The first ROI (ROI 1, 1943 pixels) corresponded to the inner part of the cylindrical container, whereas the second ROI (ROI 2, 2257 pixels) included the edges of the cylinder. In this way, two sets of values for A, B and C were obtained.

M3: Channel Ratio Method. The same two subwindows that split the photopeak window used for M2 are used here. The channel ratio method (*7*) assumes that the ratio of the number of unscattered photons detected in these two subwindows is constant as well as the ratio of the number of scattered photons, i.e.:

$$U_{lw}(i)/U_{uw}(i) = G \quad \text{and} \quad S_{lw}(i)/S_{uw}(i) = H, \quad \text{for all i}, \qquad \text{Eq. 5}$$

where U and S stand for unscattered and scattered, respectively, and lw and uw stand for lower and upper windows, respectively. The number of counts detected in the lower and the upper windows provides two other equations:

$$I_{lw}(i) = U_{lw}(i) + S_{lw}(i),$$

$$I_{uw}(i) = U_{uw}(i) + S_{uw}(i). \qquad \text{Eq. 6}$$

Consequently, calibration of G and H results in a system of four equations for four unknown values: $U_{lw}(i)$, $S_{lw}(i)$, $U_{uw}(i)$, $S_{uw}(i)$. Its solution leads to the number of unscattered photons in the photopeak window (*7*):

$$\hat{U}_{pk}(i) = (1 + G)/(G - H)[I_{lw}(i) - HI_{uw}(i)]. \qquad \text{Eq. 7}$$

Application of this method requires calibration of G and H. For each pixel, $G(i) = U_{lw}(i)/U_{uw}(i)$ and $H(i) = S_{lw}(i)/S_{uw}(i)$ were calculated. G and H were deduced as the mean value of the G(i) and H(i) values, respectively. These mean values were computed for the two ROIs (ROI 1 and ROI 2) previously described.

M4: Photopeak Energy Distribution Analysis. This method (*8*) relies on the assumption that the photopeak window can be divided into two subwindows so that for any pixel, the number of scattered photons detected within these subwindows are equal, i.e.:

$$S_1(i) = S_2(i), \qquad \text{Eq. 8}$$

where 1 and 2 label the two subwindows, with window 1 corresponding to the lowest energy range. The scatter correction consists in subtracting the image acquired in window 1 from that corresponding to window 2. This theoretically removes the scattered photons since:

$$I_2(i) - I_1(i) = U_2(i) + S_2(i) - U_1(i) - S_1(i) = U_2(i) - U_1(i). \quad \text{Eq. 9}$$

The only parameter involved in this procedure is the cutoff energy between windows 1 and 2. In order to optimize this parameter for our data, the optimal cutoff was computed for each pixel as the cutoff energy minimizing $|S_2(i) - S_1(i)|$. Its mean values for the pixels belonging to ROI 1 and ROI 2 were deduced.

M5: Dual-Energy Window Method. The dual-energy window method (*9*) assumes that the spatial distribution of the scattered photons detected in the photopeak window can be estimated by the spatial distribution of the photons detected in a secondary window, and that these two spatial distributions only differ quantitatively in a ratio k. This hypothesis is expressed by:

$$\hat{S}_{pk}(i) = kI_C(i), \quad \text{Eq. 10}$$

where I_C is the image acquired in the secondary energy window. The scatter-free image is then estimated using:

$$\hat{U}_{pk}(i) = I(i) - \hat{S}_{pk}(i), \quad \text{Eq. 11}$$

where I is the image acquired in the photopeak window. The secondary energy window was set as originally suggested, i.e., 92–125 keV. The proposed value k = 0.5 was used. In order to study the variations of k from pixel to pixel and to optimize its mean value for our data, the pixel-by-pixel values $k(i) = S_{pk}(i)/S_C(i)$ were determined. The mean value of k(i) was calculated for ROI 1 and ROI 2. The k value that scales the total amount of scatter in the secondary window to the total amount of scatter in the photopeak window, i.e.:

$$k = \sum_i S_{pk}(i) \Big/ \sum_i S_C(i), \quad \text{Eq. 12}$$

was also determined.

M6: Position-Dependent Scatter Correction Using Trapezoidal Approximation. For each pixel i, the position-dependent scatter correction method (*10*) estimates the scatter component within the photopeak window from a linear fitting of the spectrum of the photons detected in this pixel. This linear fitting is based on the numbers of photons $I_1(i)$ and $I_2(i)$ detected at energies E_1 and E_2 on both sides of the photopeak. In practice, these values are estimated by acquiring two images I_{n1} and I_{n2} corresponding to two narrow windows centred on E_1 and E_2, respectively. The linear fitting is then written:

$$\hat{S}_{pk}(i) = [I_{n1}(i) + I_{n2}(i)]w/(2w_n), \quad \text{Eq. 13}$$

where w_n and w are the widths of the narrow and photopeak windows. This means that the scatter component of the spectrum in the photopeak spectral range is estimated by the trapezoidal area located under the linear fit between E_1 and E_2. Two 2-keV wide narrow windows were used, centered on 126 and 154 keV, respectively. This method does not require any other parameter.

As Equation 13 applies to each pixel i, it also applies to the total number of scattered photons by summation over the pixels i. Consequently, if the basic hypothesis underlying the method is correct, the total number of scattered photons detected within the photopeak window, $\Sigma_i \hat{S}_{pk}(i)$, is related to the total numbers of photons detected at energies E_1 and E_2, $\Sigma_i I_1(i)$ and $\Sigma_i I_2(i)$, by:

$$\sum_i \hat{S}_{pk}(i) = \left[\sum_i I_1(i) + \sum_i I_2(i)\right] w/2. \quad \text{Eq. 14}$$

This relationship does not ensure that the basic hypothesis is correct for each pixel i. If, however, it is, then Equation 14 is true. A global assessment of the basic assumption of M6 was performed by testing the validity of Equation 14.

M7: Position-Dependent Scatter Correction Using Triangular Approximation. For each pixel i, the method estimates the number of scattered photons detected within the photopeak window from a linear fitting of the local scatter spectrum (*11*). In order to perform this linear fitting, two values of the scatter spectrum are first estimated. It is assumed that the photons detected with an energy E_2, above the photopeak (typically E_2 = 154 keV) are only unscattered photons, i.e.:

$$I_2(i) = U_2(i), \quad \text{Eq. 15}$$

where I_2 denotes the image acquired at energy E_2. It is also assumed that the photopeak is symmetrical around the emission energy E_0, i.e.:

$$U_1(i) = U_2(i), \quad \text{Eq. 16}$$

where $U_1(i)$ represents the number of unscattered photons detected in pixel i at energy $E_1 = E_0 - (E_2 - E_0)$ (E_1 = 126 keV when E_2 = 154 keV). Consequently, the number of scattered photons detected with an energy E_1 can be calculated by:

$$\hat{S}_1(i) = I_1(i) - \hat{U}_1(i) = I_1(i) - \hat{U}_2(i) = I_1(i) - I_2(i). \quad \text{Eq. 17}$$

Two values of the scatter spectrum are then known: 0 at energy E_2 and $I_1(i) - I_2(i)$ at energy E_1. The linear fit between these two values can then be deduced.

Two narrow windows, labeled n_1 and n_2 and centered on E_1 and E_2, are used to estimate $I_1(i)$ and $I_2(i)$. The number of scattered photons within the photopeak window is then given by:

$$\hat{S}_{pk}(i) = [I_{n1}(i)/w_{n1} + I_{n2}(i)/w_{n2}]w/2, \quad \text{Eq. 18}$$

where w, w_{n1} and w_{n2} are the widths of the photopeak and narrow windows.

Instead of using a trapezoid, the scatter component is estimated by the area of a right triangle with a height equal to the estimated number of scattered photons at energy E_1 and a basis corresponding to the width of the photopeak window. The narrow windows were set at 123–129 keV and 150–158 keV (*11*). No other parameters are needed.

Similar to M6, if the triangular approximation is valid for any pixel i, it can also be used to estimate the total number of scattered photons in the photopeak window from the number of photons detected with energies E_1 and E_2. The area under the true scatter spectrum and the triangular approximation were compared for a global assessment of the basic assumptions underlying the method.

M8: Constrained Factor Analysis. To estimate the image of unscattered photons, constrained factor analysis (*12*) assumes that the spectrum n_i of the photons detected in pixel i can be decomposed into a photopeak p and a Compton spectrum c with an error e_i representing noise:

$$n_i = s(i)c + u(i)p + e_i, \quad \text{Eq. 19}$$

where the scatter and photopeak spectra are normalized and s(i) and u(i) are the number of scattered and unscattered photons in pixel i. The fitting of the model proceeds in three main stages:

1. The spectra set $\{n_i\}$ is analyzed using factor analysis of medical image sequences (FAMIS) to determine two factors: a Compton factor ĉ and a photopeak + Compton factor

$\widehat{pc}$. These two factors belong to a two-dimensional study space resulting from an orthogonal decomposition of the spectra set.
2. The photopeak + Compton factor $\widehat{pc}$ is replaced by a theoretical photopeak factor $\hat{p}$.
3. The set of spectra $\{n_i\}$ is projected onto the Compton factor $\hat{c}$ and the theoretical photopeak factor $\hat{p}$ to yield the number of scattered and unscattered photons, $\hat{s}(i)$ and $\hat{u}(i)$, for every pixel i.

This method was applied using the following procedure. The spectra $\{n_i\}$ were sampled using six spectral windows: 60–68, 68–78, 78–90, 90–106, 106–126, 126–154 keV. FAMIS was carried out with an initial grouping of the neighboring pixels according to a 4 × 4 pattern. After this clustering, an automatic thresholding procedure removed the very noisy spectra to avoid disturbing the subsequent analysis. A correspondence analysis was performed as the orthogonal decomposition of the spectra which precedes the determination of the factors to remove the noise e_i. The eigenvector associated with the largest eigenvalue was used in addition to the centroid of the spectra to span the two-dimensional study space. As suggested by the authors, the theoretical photopeak was assumed to be zero from 60 to 126 keV and to be equal to 1 in the photopeak window.

By summing Equation 19 over i, the model implies that the spectrum associated with the entire image can be written as the sum of the scatter spectrum (weighted by the total number of scattered photons) and the photopeak (weighted by the total number of unscattered photons). These two spectral components were calculated and compared to the true total scatter and photopeak spectra.

M9: Factor Analysis of Medical Image Sequences Using Target-Apex Seeking (FAMIS-TAS). Although similar to approach M8, the method differs in several ways (*13*):

1. The model of spectral decomposition is more general in that it assumes that a photopeak p and several scatter spectra $\{c_k\}$ are necessary to describe any local spectrum n_i, i.e.:

$$n_i = \sum_{k=1}^{K} s_k(i)c_k + u(i)p + e_i. \qquad \text{Eq. 20}$$

2. The spectra are analyzed using a finer energy sampling.
3. The spectra c_k and p are determined in a different way. p is not assumed to be known a priori and is searched for in the study space by TAS to match the specifics of the data (e.g., energy resolution of the camera). The set of c_k is deduced by taking advantage of the previous estimation of p (*13*).

The spectra were 4 keV sampled from 60 to 180 keV. FAMIS-TAS was conducted in a similar manner to M8. An initial 4 × 4 pixel clustering was performed followed by an automatic thresholding procedure and a correspondence analysis. The eigenvectors associated with the two largest eigenvalues resulting from the correspondence analysis were used in addition to the centroid of the spectra to span a three-dimensional study space. The criterion for the TAS of p was that the photopeak should be zero from 60 to 116 keV. No information regarding the shape of the photopeak in the 116–180-keV range is required. Two Compton spectra were estimated (i.e., K = 2). The coefficients $s_k(i)$ and u(i) were computed using the projection of the initial set of spectra $\{n_i\}$ onto the spectra $\{\hat{c}_k\}$ and $\hat{p}$.

The summation of Equation 20 over the pixels i leads to the spectra associated with the entire image. The total Compton spectrum was calculated as the sum of the two scatter spectra, $\hat{c}_1$ and $\hat{c}_2$, weighted by $\Sigma_i \hat{s}_1(i)$ and $\Sigma_i \hat{s}_2(i)$, respectively. The total photopeak was $\Sigma_i \hat{u}(i)\hat{p}$. These scatter and photopeak spectra were compared with the true ones.

Comparative Assessment

For each method, relative and absolute activity quantification and the signal-to-noise ratio were assessed from the estimated scatter-free image.

Relative Activity Quantification. Five ROIs were drawn on the true image of unscattered photons. Four of them covered the inner part of the small cylinders and each one was 16 pixels in area. The fifth ROI (1285 pixels) was drawn over the background.

Since the geometry of the simulated phantom is perfectly known as well as the attenuating medium (water), the relationship connecting the ratio k_i of activity concentration between a cylinder i and the background with the mean numbers of counts per pixel in ROI i and in the background ROI, A_i and A_0, can be analytically derived:

$$k_i = 6.558\,(A_i - A_0)/A_0 + 1. \qquad \text{Eq. 21}$$

It takes into account the attenuation affecting the projection. Consequently, for a projection containing only unscattered photons, the theoretical values of k_i for the four cylinders are 2, 4, 6 and 8.

Absolute Activity Quantification. The accuracy of absolute activity quantification was assessed by plotting the estimated number of unscattered photons against the true number for every pixel i in which the true value exceeded 30. The correlation coefficients r associated with these plots were calculated as a measure of their spread.

The absolute value of the relative error defined as:

$$\varepsilon(i) = |\hat{U}(i) - U(i)| * 100/U(i), \qquad \text{Eq. 22}$$

was calculated for each pixel i and represented as a function of the true number of unscattered photons in pixel i, U(i).

Signal-to-Noise Ratio. The signal-to-noise ratio was calculated from the background ROI by:

$$SNR = m/sd, \qquad \text{Eq. 23}$$

where sd and m are the standard deviation and mean of $\{\hat{U}(i)\}$ in the ROI.

RESULTS

Scatter Correction Methods

M1. The photopeak image contains 1,395,752 events with 30.6% as scattered photons. Multiple scattered photons represent 18.5% of the scattered photons and 2.1% of the unscattered photons detected within the 60–180-keV range fall outside the photopeak window.

M2. The plots of the scatter fractions against the ratio of the number of events falling into two subwindows, lw and hw, are represented in Figure 2 for ROI1 and ROI2, as are the results of the fits. The parameters A, B and C are equal to:

ROI 1: A = −0.359 B = −1.451 C = 0.629,

ROI 2: A = 0.015 B = 4.628 C = 0.323.

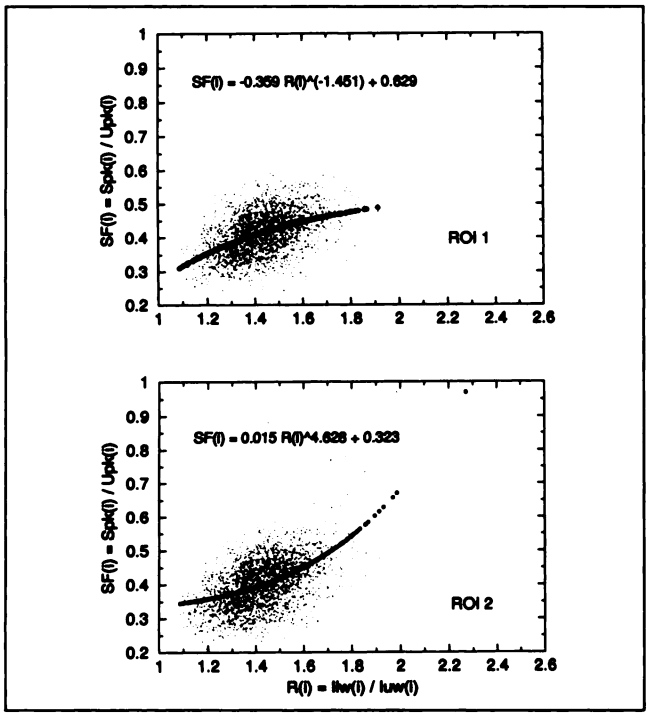

FIGURE 2. Plots of the scatter fractions SF(i) against the ratio R(i) of the number of counts falling into the two equally wide subwindows splitting the photopeak window. Each point corresponds to a pixel i. The results of the fitting $SF(i) = A\ R(i)^B + C$ when pixels belonging to ROI 1 and ROI 2 are also shown.

It should be noted that the curvatures of the two fitting curves differ. This leads to a different estimation of scatter, especially for pixels in which R(i) is low (<1.2) or high (>1.6). The corrections were performed using these two sets of values, leading to two corrected images, subsequently denoted M2 and M2*.

M3. Figure 3 shows the distributions of G(i) and H(i) values. For ROI 1 and ROI 2, the mean value, standard deviation, minimum and maximum values of these two parameters are:

ROI 1: G = 1.02 sd = 0.10 min = 0.74 max = 1.41
H = 3.85 sd = 0.78 min = 2.30 max = 7.93
ROI 2: G = 1.03 sd = 0.10 min = 0.59 max = 1.43
H = 3.85 sd = 0.80 min = 2.14 max = 7.93

Because G and H mean values derived from the two ROIs do not significantly differ, the values G = 1.03 and H = 3.85 were chosen for the correction.

M4. For both ROIs, the mean optimal cutoff between windows 1 and 2 is 134.5 keV:

window 1: 126–134 keV and window 2: 135–154 keV.

The optimal cutoff corresponding to individual pixels varies between 132.5 and 136.5 keV. For mean optimal cutoff, the number of scattered photons $S_2(i)$ in the upper window is plotted against the number of scattered photons $S_1(i)$ in the lower window (Fig. 4A). Although this cutoff is optimal for a processed image, the scatter contents of the lower window tend to be higher than those of the upper window. The number of unscattered photons $U_1(i)$ in the lower window is represented as a function of the number of unscattered photons $U_2(i)$ in the upper window in Figure 4B. A linear regression leads to:

$$U_1(i) = 0.218\ U_2(i) + 0.655 \qquad (r = 0.964). \quad \text{Eq. 24}$$

This means that when 100 unscattered photons are detected in subwindow 2, about 22 are detected in subwindow 1. Consequently, for our experiment, the correction typically results in ~18% removal of unscattered photons with respect to those detected in the photopeak window.

M5. Analysis of the spectral contents of the secondary energy window 92–125-keV indicates that 99% of the detected photons are scattered photons and 55% of those photons are multiple scattered, whereas in the photopeak window only 18.5% of the scattered photons have undergone multiple scattering.

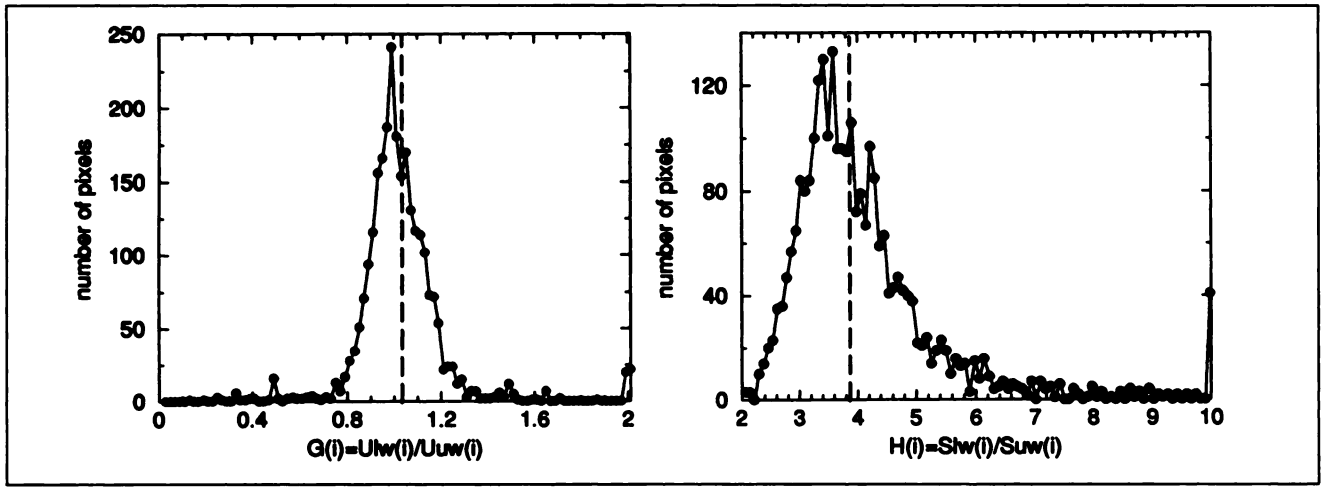

FIGURE 3. Histograms of G(i) and H(i) values for the channel ratio method. The dashed lines represent the values used for the correction (G = 1.03, H = 3.85).

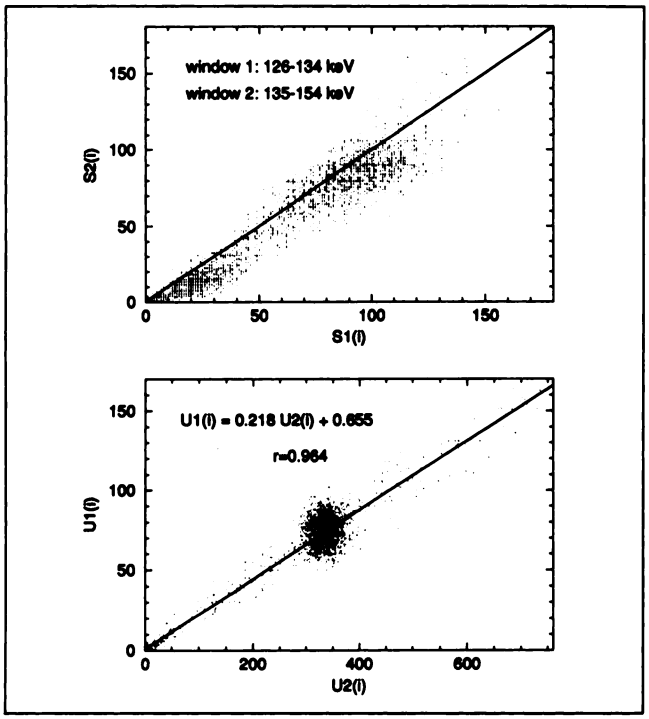

FIGURE 4. (A) Plot of the number of scattered photons $S_2(i)$ in the upper window against the number of scattered photons $S_1(i)$ in the lower window. Each point corresponds to a pixel i. The solid line corresponds to $S_2(i) = S_1(i)$. (B) Plot of the number of unscattered photons $U_1(i)$ against the number of unscattered photons $U_2(i)$ in the upper window. Each point corresponds to a pixel i. The solid line corresponds to the linear regression result.

Figure 5 shows the distribution of k(i) values. The analysis of k(i) values within both ROI 1 and ROI 2 leads to:

ROI 1: k = 0.55 sd = 0.06 min = 0.36 max = 0.80,

ROI 2: k = 0.55 sd = 0.06 min = 0.34 max = 0.80.

The correction was performed with the conventional value 0.5, as well as with the mean value 0.55. Two corrected images, referred to as M5 and M5*, were thus obtained. The value of k that makes the number of scattered photons in the secondary window equal to the number of scattered photons in the photopeak window is 0.53.

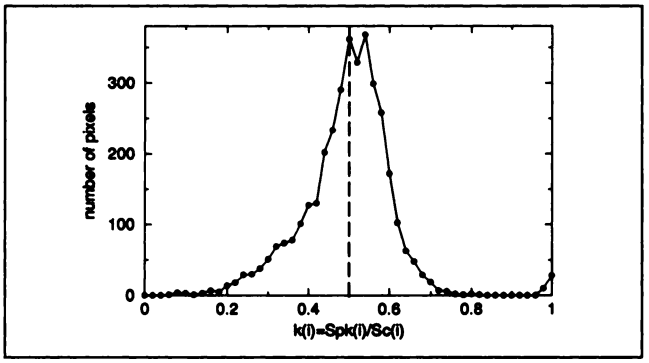

FIGURE 5. Histogram of the k(i) values for the dual-energy window method. The dashed line represents k = 0.5.

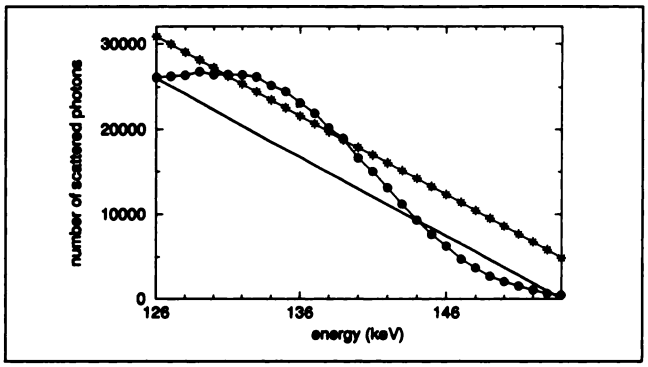

FIGURE 6. Total scatter spectrum (•) in the photopeak window, trapezoidal approximation (*) and triangular approximation (—).

M6. Figure 6 shows the exact total scatter spectrum within the photopeak window along with the linear fit based on the number of events detected at 126 and 154 keV. The true number of scattered photons, corresponding to the area under the true scatter spectrum, is 440,217. The estimated number of scattered photons, corresponding to the trapezoidal area, is 518,273, representing an overestimation of ~18%.

M7. Triangular approximation (Fig. 6) was used to estimate the numbers of scattered photons, which is 376,841, whereas the true area under the scatter spectrum is 440,217. The linear fit results in an underestimation of ~14%.

For the different assumptions of the method, we found that:

1. If the number of scattered photons at 126 and 154 keV were accurately estimated, the linear fitting of the spectrum between these two energies would lead to an underestimation of ~12.5% of the scatter contents.
2. For an energy equal to 154 keV, ~10% of the detected photons are scattered photons.
3. The relative difference between the number of unscattered photons detected at 126 and 154 keV is ~8%.

M8. The last step of the model fitting (i.e., the projection onto the estimated spectra) results in a photopeak image including 1,803,217 events and a scatter image containing 1,126,613 events. The projection also results in 518 "negative events," i.e.

$$\sum_i s^-(i) + \sum_i u^-(i) = -518,$$

where $u^-(i)$ and $s^-(i)$ denote negative values of u(i) and s(i).

Consequently, the total number of "restored" events is 2,929,312, whereas 2,965,582 events were initially analyzed. This discrepancy (loss of ~1.2% events) shows that the fitting of the model does not restore the correct number of events and is "quantitatively inconsistent" (as discussed below).

The estimated Compton spectrum and the theoretical

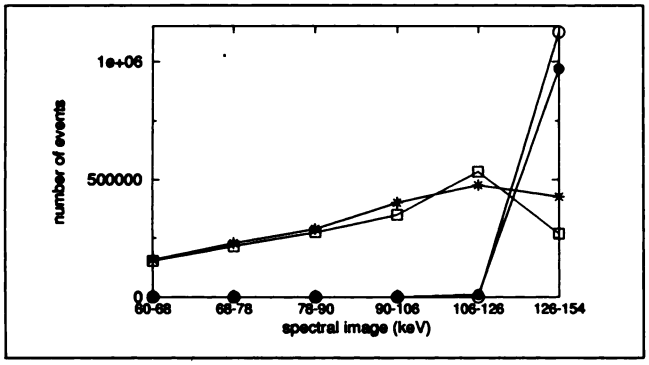

FIGURE 7. True scatter (•), photopeak spectra (•) and results of estimation using constrained factor analysis (r scatter, o photopeak).

photopeak corresponding to the spectral sampling used for the constrained factor analysis are shown in Figure 7, as are the exact scatter and photopeak spectra. The true photopeak is actually zero from 60 to 106 keV. Only 1.1% of the unscattered photons are detected in the 106–126 window, whereas M7 assumes that all unscattered photons are detected within the 126–154 photopeak window.

M9. This method results in a photopeak image, including 1,092,176 events and two scatter images including 1,436,701 and 517,579 events, respectively; 60,944 "negative events" are observed. The total number of restored events is thus 2,985,512, whereas 2,985,547 events were initially processed. The difference between these two numbers is due only to roundoff errors, and M9 appears to be "quantitatively consistent."

The estimated and true spectral components are shown in Figure 8.

Comparative assessment

Relative Activity Quantification. The concentration ratios calculated for the different corrected images are plotted against the true concentration ratios in Figure 9. Several behaviors can be distinguished for relative activity quantification:

1. M1 and M2 underestimate activity concentration ratios. The greater the initial ratio, the greater the underestimation.

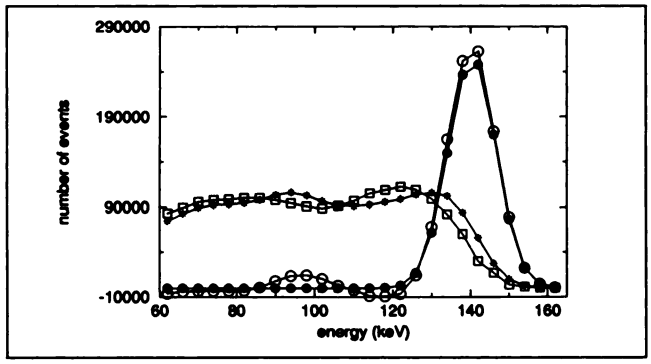

FIGURE 8. True scatter (•), photopeak spectra (•) and estimation results from FAMIS-TAS (r = scatter, o = photopeak).

2. M3, M4, M5 and M6 overestimate activity concentration ratios. For M4 and M5, the greater the initial ratio, the greater the overestimation. Unlike M4 and M5, the degree of overestimation does not vary regularly with the initial ratio for M3 and M6.
3. M7, M8 and M9 lead to satisfactory relative activity quantification and do not introduce a bias (e.g., over- or underestimation for any initial ratio).

Absolute Activity Quantification. The plots of the estimated numbers of unscattered photons against the true numbers are shown in Figure 10. M1 and M4 rule out absolute activity quantification. M2 introduces a bias: it overestimates the number of unscattered photons U(i) when this number is low and then tends to underestimate it. M2* (data not shown) has the same result with smaller bias, however, M3 and M6 yield strong spread plots along the y-axis. The global location of the cloud of points is not far from the identity line, but the spread of the points induces local errors. These spreads indicate high noise in the corrected images. The plots corresponding to M5 and M5* (data not shown) are very close to the identity line. For M5, a slight bias can be seen, namely an underestimation for low U(i) values and an overestimation for high U(i) values. M5* displays an underestimation up to U(i) ≈ 480 and a slight overestimation from U(i) ≈ 680. M7 allows absolute activity quantification up to U(i) ≈ 380, and overestimates the number of unscattered photons for superior U(i) values globally. M8 and M9 plots show similar tendencies, i.e., a global overestimation of U(i), slightly more pronounced in the case of M8 than with M9.

The analysis of the absolute values of the relative error ε (Fig. 11) gives more specific information about the quantitative performance of the different methods. Figure 11 confirms that M1 and M4 do not permit absolute activity quantification. For M2 and M2*, ε is low and depends little on the parameters for U(i) > 130. When U(i) < 130, ε increases markedly up to 80% for M2, whereas this increase is less pronounced for M2*. M3 leads to a low error when U(i) > 130, which goes up when U(i) < 130 and reaches ~40% when U(i) ≈ 35. In the dual-energy window method (M5 and M5*), the relative error depends upon k but remains close to 5% and inferior to 10% when U(i) > 180. The error increases notably when U(i) < 180 and then becomes more dependent upon k. With M6, ε is ~10% when U(i) exceeds 330, and increases up to 45% for lower U(i) values. M7 also introduces an error of ~10% for a wider range of U(i) values. When U(i) < 130, the error rises up to ~35%. The error with M8 is ~10%–15% when U(i) > 130. As for the previous methods, it increases for lower values. Finally, an error of ~10% is observed with M9 when U(i) > 130. Unlike the other methods, however, the error does not increase very much for lower U(i) values and the maximum error is ~25% when U(i) ≈ 35.

Signal-to-Noise Ratios. The signal-to-noise ratios corresponding to the corrected images are reported in Table 1. Three methods (M3, M4, M6) yield images with poor sig-

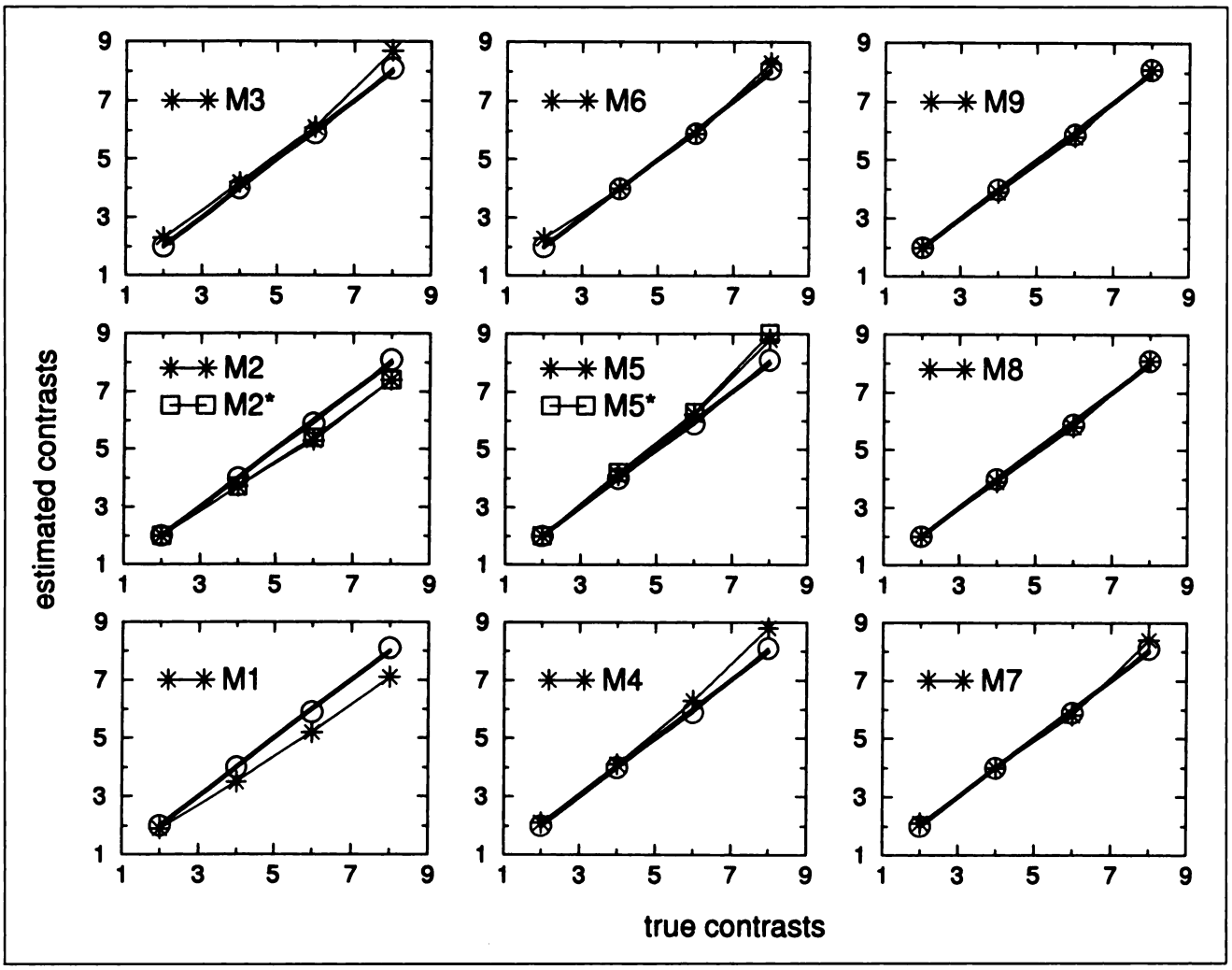

FIGURE 9. Concentration ratios calculated for the different corrected images against true concentration ratios. Identity line (—); values measured on the true image of unscattered photons (○).

nal-to-noise ratios ($9 < SNR < 10.5$). The ratios are high and only slightly lower than the signal-to-noise ratio of the true image of unscattered photons (20.1) with four methods (M1, M2 and M2*, M8, M9). Intermediate signal-to-noise ratios are obtained with M5, M5* and M7. Table 1 summarizes the performance of the different methods.

DISCUSSION

The strength of the Monte Carlo approach is that it allows us to investigate the intrinsic performance of the scatter correction methods by separating effects caused by scatter from other effects, such as those related to limited spatial resolution, attenuation or reconstruction. We report the quantitative results of the methods for a particular geometry and for perfect experimental conditions (e.g., without uniformity defects). They cannot be readily extrapolated to what would happen when those methods are combined with techniques that compensate for attenuation or spatial response function. These other corrections (or lack of correction) will affect quantification as well and should also be considered. We believe, however, that a better understanding of the contribution of different factors to the overall error is facilitated by studies addressing each issue individually. This should help focus on the major sources of error in the quantification process and allow better understanding of how different error sources may be partially cancelled or amplified.

Nonquantitative Methods

Two methods enable neither relative nor absolute activity quantification: photopeak window acquisition (M1) and photopeak energy distribution analysis (M4). About 30% of the photons detected in the 20% photopeak window are scattered photons. Even with ^{99m}Tc when no high-energy photons are emitted in addition to the main photopeak, ~20% of scattered photons detected within the photopeak window result from multiple scattering. Consequently, the quantitative potential of any scatter correction method relying on the hypothesis of single scattering is restricted. Photopeak energy distribution analysis performs somewhat better than photopeak window acquisition in that it amplifies contrast, which may be desirable for detecting

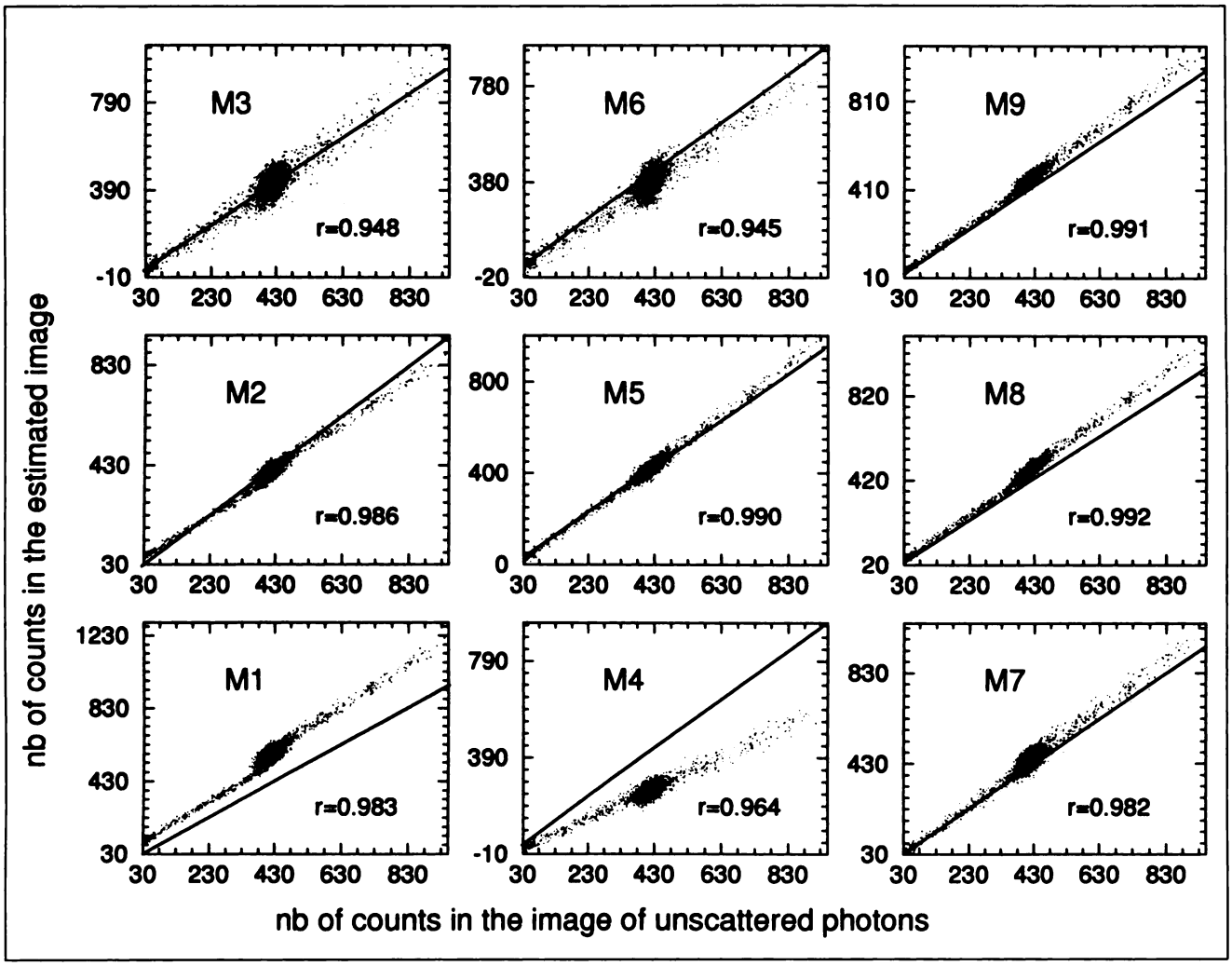

FIGURE 10. Plots of the estimated numbers of unscattered photons against the true numbers. Each point corresponds to a pixel i. Identity line (—); r = correlation coefficient associated with the plot.

lesions. The corrected image, however, is very noisy due to the removal of ~20% unscattered photons. This removal is inherent in the method's foundation and cannot make it competitive for quantitative purpose.

Methods Requiring Calibration

The dual photopeak window method (M2) relies on the calibration of parameters A, B and C. Our study shows that the relationship between the scatter fraction SF(i) and the ratio R(i) of the number of photons detected within the two subwindows splitting the photopeak is not well defined. It is far from clear whether the fit suggested by the authors is the best. The correction is globally not very sensitive to the values of the parameters because local errors occur in any case. The sensitivity of the method to its parameters A, B and C essentially appears for extreme low and high values of R(i), which represent only a small portion of pixels. Because the method tends to overestimate the number of unscattered photons when it is low and to underestimate it when it is high (Fig. 10), the activity ratios between different ROIs are underestimated. The local errors introduced by the method, together with the bias for extreme low and high U(i) values, are particularly awkward because the lesions which are due to be detected and quantified usually correspond to local areas with abnormal uptake, i.e., extreme U(i) values.

The channel ratio method (M3) requires the calibration of G and H. As was theoretically expected, G approximately follows a Gaussian distribution around a value close to 1. The distribution of H, however, is skewed to the right. This means that in the 126–154 keV range, the shape of the scatter spectrum varies from pixel to pixel. This observation agrees with the fact that the photopeak window includes single and multiple scattered events. As the proportion of single and multiple scatter may vary from one pixel to another, the shape of the scatter spectra associated with different pixels also varies. On the average, a good fit is observed between the identity line and the plot $\hat{U}(i)$ against U(i). The cloud of points, however, is markedly spread, which shows that the corrected image is noisy (SNR = 9.6, against 20.1 in the true image of unscattered photons).

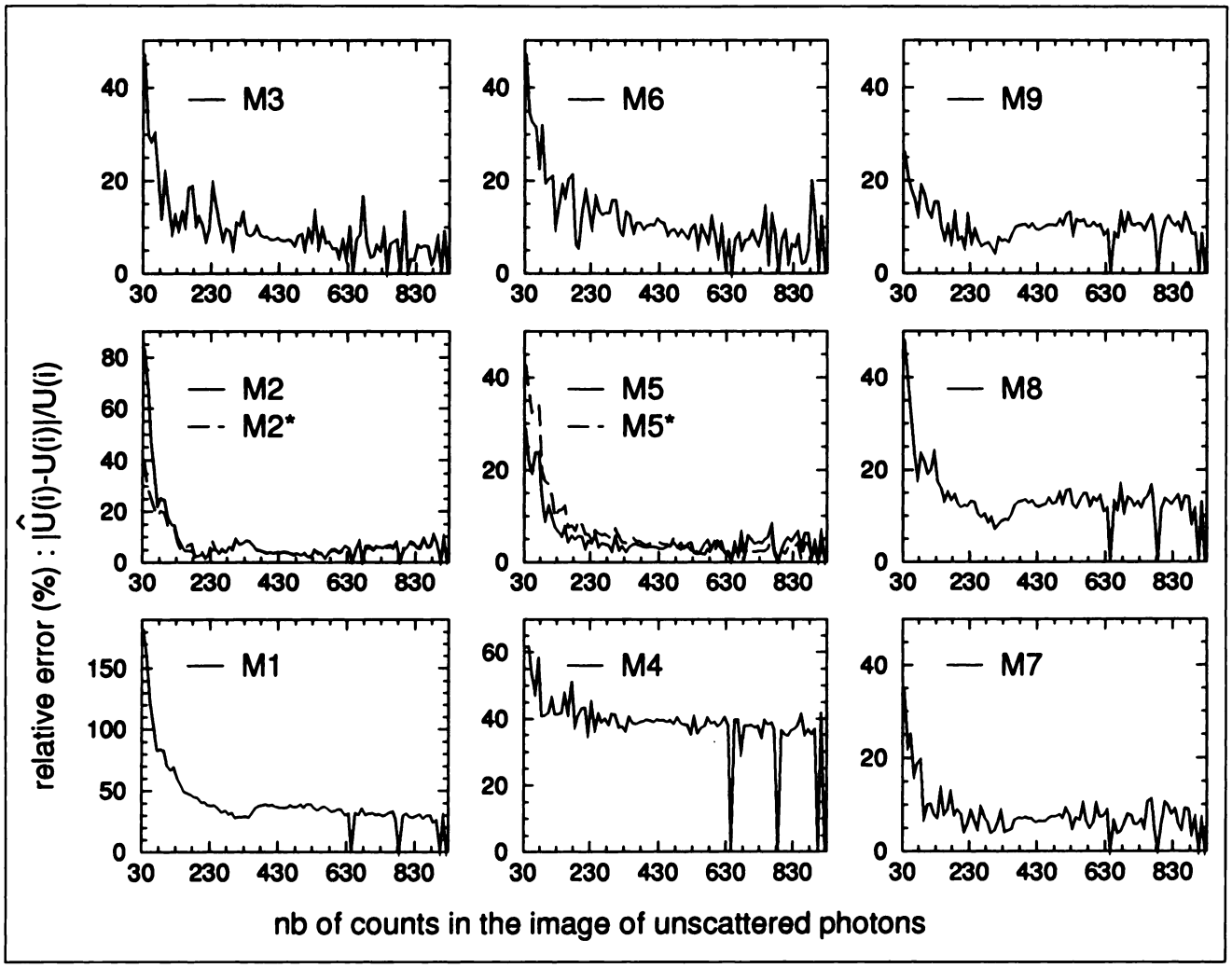

FIGURE 11. Histograms of the relative errors as a function of number of unscattered photons per pixel for each scatter correction methods.

The dual-energy window method was applied by using both the commonly accepted value k = 0.5 and a k value derived from a more comprehensive analysis of our data. The results show that k = 0.5 is a reasonable choice for the simulated phantom. The accuracy of the method is limited by the difference between the spatial distribution of the scattered photons detected within the secondary window and that of the scattered photons detected within the photopeak window. For instance, the proportion of multiple scattered photons is much greater in the secondary window (55%) than in the photopeak window (18.5%). As the scatter component associated with the secondary window accounts for higher order scatter or greater angle scatter than the component associated with the photopeak window, the subtraction results in an overcorrection far from the source location, and an undercorrection near the source. Low activity areas will then contain too few events and high activity areas will contain too many photons. This results in an enhancement of contrast which makes relative activity quantification misleading.

It is also worth noticing that whereas k = 0.5 leads to a global overestimation of the unscattered contents within the photopeak window, this error is partially cancelled by using the total number of unscattered photons in the 60–180 keV range as the true reference U(i) rather than the number of unscattered photons in the photopeak window. This slight difference (only 2.1% of unscattered photons are detected outside the photopeak window) does not significantly affect absolute activity quantification results. Nevertheless, it can influence the results properly when the method yields an overestimation of the number of unscattered photons in the photopeak window (e.g., M5, M7).

Methods Involving Linear Fitting

The trapezoidal approximation (M6) globally overestimates the number of scattered photons in the photopeak window. This proves that this approximation will also turn out to be locally erroneous, as demonstrated in Figure 11. Due to the narrow windows used, the method results in a noisy image (SNR = 9, r = 0.945) which hinders accurate local quantification.

Unlike trapezoidal approximation, triangular approxi-

TABLE 1
Summary of the Performance of Nine Scatter Correction Methods

	Method	Requires parameter(s)	Relative quantification	Absolute quantification for high U	Absolute quantification for low U (30 < U < 130)	SNR	Number of spectral windows
M1	Photopeak window acquisition	no +	poor −	poor − ε > 30%	poor − ε > 65%	good + 19.2	1 +
M2	Dual photopeak window	yes −	poor −	good + ε < 10% for U > 130	approx. 10% < ε < 80%	good + 19.6; 18.9	2
M3	Channel ratio	yes −	poor −	good + ε ~ 10% for U > 130	approx. 10% < ε < 45%	poor − 9.6	2
M4	Photopeak energy distribution analysis	yes −	poor −	poor − ε ~ 40%	poor − ε > 40%	poor − 10.5	2
M5	Dual-energy window	yes or no	poor −	good + ε ~ 5% for U > 230	approx. 15% < ε < 45%	inter. 14.9; 15.9	2
M6	Trapezoidal approximation	no +	approx.	good + ε ~ 10% for U > 330	approx. 10% < ε < 45%	poor − 9.0	3
M7	Triangular approximation	no +	approx.	good + ε < 10% for U > 130	approx. 5% < ε < 35%	inter. 14.1	3
M8	Constrained factor analysis	no +	good +	approx. ε < 15% for U > 130	approx. 20% < ε < 50%	good + 18.8	6 (list-mode) −
M9	FAMIS-TAS	no +	good +	good + ε ~ 10% for U > 130	approx. 10% < ε < 25%	good + 17.8	30 (list-mode) −

+ = merit; − = inconvenience; ε = relative error; U = short for the number of unscattered photons per pixel U(i); approx. = approximate; and inter. = intermediate.

mation (M7) underestimates the number of scattered photons in the photopeak window. The linear fit does not permit a proper estimation of the integral of the scatter spectrum between 126 and 154 keV (~12.5% underestimation of the number of scattered photons). Moreover, since some scattered photons are detected with an energy equal to 154 keV, the deduced number of scattered photons detected at an energy equal to 126 keV is underestimated. This also contributes to the global underestimation of the number of scattered photons. The wider spectral windows make the method less sensitive to noise (SNR = 14.1, r = 0.982) than M6.

Factor Analysis Methods

These methods have been applied using an automatic thresholding procedure and a correspondence analysis as the orthogonal decomposition. In this way, they essentially differ in the model (one or two scatter spectra) and in the technique used to estimate the basis spectra. The constrained factor analysis described (*12*) did not use an automatic thresholding and used principal component analysis instead of correspondence analysis. However, the automatic thresholding proposed as part of M9 has been used for M8 so that differences in results cannot be attributed to differences in thresholding procedures. As correspondence analysis has been demonstrated to be the optimal orthogonal decomposition for scintigraphic data (*14*), it has been used for both M8 and M9.

Our main aim was to study the differences between M8 and M9 resulting from the differences in the models and in the procedures used to estimate the basis spectra. Two weaknesses of the constrained factor analysis (M8) have been shown. First, modeling each local spectrum by the weighted sum of a photopeak and a scatter spectrum does not permit a precise description of the spectra. The estimated total scatter spectrum departs significantly in shape from the original one. Indeed, in the wide spectral range which is considered, the scatter spectrum corresponding to each pixel differs from pixel to pixel and cannot be described by a single shape scaled by a coefficient. On the other hand, the modeling of the photopeak is reasonable given the spectral sampling. A second problem is related to conservation of processed information. After the correction, the sum of the signal assumed to be scatter and unscatter differs from the total signal initially processed. This inconsistency results from the substitution of the theoretical photopeak for the estimated photopeak + scatter spectrum. Since the theoretical photopeak does not belong to the study space resulting from the orthogonal decomposition, the final projection is inconsistent. Despite these two problems, the method performs rather well for relative activity quantification and signal-to-noise ratios. Absolute activity quantification, however, suffers from a global overestimation.

The alternative method of factor analysis (M9) does not present the problem of loss of part of the processed signal, because the basis spectra (c_k) and p used for modeling the

local spectra (Eq. 20) belong to the study space. The final projection is then consistent. The comparison of the estimated total scatter and photopeak spectra with the original ones shows an overall correct estimation.

Some discrepancies, however, are observed in the shape of the low-energy tail of the photopeak and in the total scatter spectrum. There are two possible explanations: A three-dimensional study space was used to analyze the data and to estimate the basis spectra $\{c_k\}$ and p. This could be insufficient for a precise description of the spectra given the fine sampling. The benefits from using a larger study space or a coarser sampling have to be investigated. The second problem encountered by FAMIS-TAS is that several sets of basis spectra can usually be found in the study space, and are compatible with a correct description of the data given some a priori constraints (e.g., c_k, p, $s_k(i)$ and u(i) have to be positive or zero for the model to have a physical meaning). These different sets of basis spectra lead to different scatter and photopeak images. The determination of the basis which is the most appropriate for separating scattered from unscattered photons still has to be worked out. It could require consideration of other constraints. FAMIS-TAS leads to results which are slightly better than those obtained with constrained factor analysis. Although fine sampling was used, the signal-to-noise ratio in the corrected image is high because of the correspondence analysis, which filters the initial spectra and permits robust estimation of the basis spectra from the noise-free portion of the spectra (*14*). Overall overestimation in absolute activity quantification is observed. A remarkable feature of FAMIS-TAS is that it performs almost equally well over a wide range of U(i) values (i.e., the quantification is as reliable for cold areas or low counting statistics as for hot areas or high counting statistics). This results from the absence of parameters derived from the mean shape of the spectra or from the mean contents of the pixels.

Both factor analyses do not require the calibration of parameters. Unlike M2, M3, M4 and M5, no parameters were optimized given the data that had to be processed. In this respect, these approaches are appealing since they result in an overall satisfactory correction, especially regarding relative activity quantification.

Sensitivity of the Methods to Camera Uniformity

Among the methods of spectral analysis that we evaluated, three of them, namely M5, M8 and M9, use a wide spectral range while the others rely essentially on spectral analysis in the photopeak window. The camera response is usually optimized for the standard photopeak window acquisitions. Consequently, those methods that rely on a spectral range far from the photopeak window may be affected by spectral nonuniformity in that range. It can be expected that the finer the energy sampling, the more sensitive the method will be to nonuniformity defects. Indeed, when coarse sampling is used (i.e., wide spectral windows) spectral nonuniformities may be cancelled. In that respect, methods M8 and M9 will be the more sensitive to camera nonuniformity since they rely on both wide spectral range and fine sampling. Preliminary investigations show promising results on the possibility of obtaining stable spectral responses over a wide spectral range (*15*).

CONCLUSION

We have studied the performance of nine scatter correction methods in optimal experimental conditions. The photopeak acquisition and the photopeak energy distribution analysis allow neither relative nor absolute quantification and should not be considered further when aiming at quantification. Among the methods requiring parameter calibration (M2, M3, M5), the dual-energy window method is a good compromise. It is simple because a default k value can be used, and the results are equally good or better than with M2 or M3. The very principle of M5 makes it less sensitive to possible nonuniformity of the spectral response of the camera than M2 and M3. The dual-energy window method introduces a bias in relative activity quantification, however, by underestimating the activity in low activity areas and overestimating it in high activity areas.

Concerning the methods relying on spectral analysis based on measurement of two values of the local spectra (M6, M7), the triangular approximation performs better than the trapezoidal approximation. It is a valuable alternative to the dual-energy window method, especially for relative activity quantification. On the other hand, it leads to noisier images because it uses narrower spectral windows than M5.

FAMIS-TAS (M9) is preferable to the constrained factor analysis (M8), both theoretically and practically. It enables satisfactory relative activity quantification over a wide range of activity, but still needs to be improved for absolute activity quantification. The relative error is about 10% in optimal experimental conditions. This study was performed for ^{99m}Tc because most scatter corrections address ^{99m}Tc acquisitions. Scatter is also of great concern when imaging isotopes with more complex spectra, especially those emitting high energy photons in addition to the main photopeak (^{67}Ga, ^{201}Tl, etc.). For those radioisotopes, FAMIS-TAS is the most appealing method since, unlike the other methods, the methodology applies with only few changes (*16*).

ACKNOWLEDGMENTS

This work has been supported by a grant from the Association pour la Recherche sur le Cancer, Villejuif, France.

REFERENCES

1. Buvat I, Benali H, Todd-Pokropek A, et al. Scatter correction in scintigraphy: the state of the art. *Eur J Nucl Med* 1994;21:675–694.
2. Raeside DE. Monte Carlo principles and applications. *Phys Med Biol* 1976; 21:181–197.
3. Nelson WR, Rogers DWO. The EGS4 code system. In: Jenkins TM, Nelson WR, Rindi A, eds. *Monte Carlo transport of electrons and photons*. New York and London: Plenum Press; 1988:287–342.
4. Rodriguez-Villafuerte M. *The use of transmission-emission computed tomography for improved quantification in SPECT*. PhD Thesis, University College London, 1994.

5. Knoll GF. *Radiation detection and measurement*. New York: Wiley; 1989: 287–336.
6. King MA, Hademenos GJ, Glick SJ. A dual-photopeak window method for scatter correction. *J Nucl Med* 1992;33:605–612.
7. Pretorius PH, van Rensburg AJ, van Aswegen A, et al. The channel ratio method of scatter correction for radionuclide image quantitation. *J Nucl Med* 1993;34:330–335.
8. Logan KW, McFarland WD. Single photon scatter compensation by photopeak energy distribution analysis. *IEEE Trans Med Imag* 1992;11:161–164.
9. Jaszczak RJ, Floyd CE, Coleman RE. Scatter compensation techniques for SPECT. *IEEE Trans Nucl Sci* 1985;32:786–793.
10. Ogawa K, Harata Y, Ichihara T, et al. A practical method for position-dependent Compton-scattered correction in Single Photon Emission CT. *IEEE Trans Med Imag* 1991;10:408–412.
11. Bourguignon MH, Wartski M, Amokrane N, et al. Le spectre du rayonnement diffusé dans la fenêtre du photopic: analyse et proposition d'une methode de correction. *Médecine Nucléaire* 1993;17:53–58.
12. Mas J, Hannequin P, Ben Younes R, et al. Scatter correction in planar imaging and SPECT by constrained factor analysis of dynamic structures (FADS). *Phys Med Biol* 1990;35:1451–1465.
13. Buvat I, Benali H, Frouin F, et al. Target apex-seeking in factor analysis of medical image sequences. *Phys Med Biol* 1993;38:123–138.
14. Benali H, Buvat I, Frouin F, et al. A statistical model for the determination of the optimal metric in Factor Analysis of Medical Image Sequences (FAMIS). *Phys Med Biol* 1993;38:1065–1080.
15. Buvat I, Benali H, Todd-Pokropek A, et al. A new correction method for gamma camera nonuniformity due to energy response variability. *Phys Med Biol* 1995; in press.
16. Buvat I, Benali H, Di Paola R. Answer to the question of the month. *Nucl Med Commun* 1994;15:306.